

Electronic phase diagram of iron chalcogenide superconductors $\text{FeSe}_{1-x}\text{S}_x$ and $\text{FeSe}_{1-y}\text{Te}_y$

Shaobo Liu^{1,2}, Jie Yuan^{1,5,6}, Soonsang Huh^{3,4}, Hanyoung Ryu^{3,4}, Mingwei Ma^{1,6}, Wei Hu^{1,2}, Dong Li^{1,2}, Sheng Ma^{1,2}, Shunli Ni^{1,2}, Peipei Shen^{1,2}, Kui Jin^{1,2,5,6}, Li Yu^{1,2,6*}, Changyoung Kim^{3,4}, Fang Zhou^{1,2,6*}, Xiaoli Dong^{1,2,5,6*}, Zhongxian Zhao^{1,2,5,6}

¹ *Beijing National Laboratory for Condensed Matter Physics and Institute of Physics, Chinese Academy of Sciences, Beijing 100190, China*

² *School of Physical Sciences, University of Chinese Academy of Sciences, Beijing 100049, China*

³ *Center for Correlated Electron Systems, Institute for Basic Science, Seoul 08826, Republic of Korea*

⁴ *Department of Physics and Astronomy, Seoul National University, Seoul 08826, Republic of Korea*

⁵ *Key Laboratory for Vacuum Physics, University of Chinese Academy of Sciences, Beijing 100049, China*

⁶ *Songshan Lake Materials Laboratory, Dongguan, Guangdong 523808, China*

* Correspondence to: fzhou@iphy.ac.cn (F.Z.); li.yu@iphy.ac.cn (L.Y.); dong@iphy.ac.cn (X.L.D.)

Abstract

Here we establish a combined electronic phase diagram of isoelectronic $\text{FeSe}_{1-x}\text{S}_x$ ($0.19 \geq x \geq 0.0$) and $\text{FeSe}_{1-y}\text{Te}_y$ ($0.04 \leq y \leq 1.0$) single crystals. The $\text{FeSe}_{1-y}\text{Te}_y$ crystals with $y = 0.04 - 0.30$ are grown by a hydrothermal ion-deintercalation (HID) method. Based on combined experiments of the specific heat, electrical transport, and angle-resolved photoemission spectroscopy, no signature of the tetragonal-symmetry-broken transition to orthorhombic (nematic) phase is observed in the HID $\text{FeSe}_{1-y}\text{Te}_y$ samples, as compared with the $\text{FeSe}_{1-x}\text{S}_x$ samples showing this transition at T_s . A ubiquitous dip-like temperature dependence of the Hall coefficient is observed around a characteristic temperature T^* in the tetragonal regimes, which is well above the superconducting transition. More importantly, we find that the superconducting transition temperature T_c is positively correlated with the Hall-dip temperature T^* across the $\text{FeSe}_{1-x}\text{S}_x$ and $\text{FeSe}_{1-y}\text{Te}_y$ systems, suggesting that the tetragonal background is a fundamental host for the superconductivity.

- **Introduction.** The superconductivity in iron chalcogenide Fe(Te,Se) emerges as the long-range antiferromagnetic (AFM) order in the parent compound FeTe is suppressed¹, similar to the superconductivity in iron pnictides^{2,3}. The non-magnetic iron chalcogenide FeSe superconductor is unusual in that a nematic electronic order has been observed⁴⁻⁹, which is associated with a rotational-symmetry-breaking transition from a tetragonal to an orthorhombic phase at $T_s \sim 90$ K. The superconductivity in FeSe coexists with the nematic order, and shows a rather low transition temperature T_c (~ 9 K). Nevertheless, the superconductivity can be strongly enhanced by high pressure ($T_c \sim 38$ K), chemical intercalation ($T_c \sim 30 - 50$ K), or fabrication of monolayer FeSe ($T_c \sim 65$ K). The nematicity is completely suppressed in these cases, and significant doping effects can also be involved. Tuning the superconducting (SC) and electronic properties by the isovalent substitutions of chalcogen elements S and Te for Se in FeSe is a pristine way to probe the origin of superconductivity, with the doping effect reduced to minimum. The resultant FeSe_{1-x}S_x¹⁰ and FeSe_{1-y}Te_y¹¹⁻¹³ series consist only of the superconducting/conducting blocks each comprising one iron plane sandwiched between two chalcogen planes, in absence of the interlayers of guest atoms or molecules. Therefore, these simple iron-based compounds provide a unique platform to investigate the intrinsic ingredients for the unconventional superconductivity in a wide isoelectronic phase region. Particularly, it is highly desirable to obtain experimental evidence for the link between the superconductivity and normal-state electronic property by tracking their respective dependences on the isovalent substitution.

In this study, we succeed in synthesizing a series of tellurium-substituted FeSe_{1-y}Te_y single crystals, covering the substitution range of $0.04 \leq y \leq 0.30$, by our recently developed hydrothermal ion-deintercalation (HID) method¹⁴. Single crystals of sulfur-substituted FeSe_{1-x}S_x with $x = 0$ (FeSe), 0.07 and 0.13, and FeSe_{1-y}Te_y with higher $y = 0.61, 0.89$ and 1.0, are also obtained by chemical-vapor-transport (CVT) method^{15,16} and self-flux growth¹⁷ with post annealing¹⁸, respectively. Further, we establish a combined phase diagram of FeSe_{1-y}Te_y ($0.04 \leq y \leq 1.0$) and FeSe_{1-x}S_x ($0.19 \geq x \geq 0.0$) systems based on systematic characterizations. Contrasting with the presence of the

orthorhombic/nematic phase below T_s in stoichiometric FeSe and substituted FeSe_{1-x}S_x, no signature of the electronic nematicity is detectable in the HID FeSe_{1-y}Te_y samples from the specific heat and electrical transport measurements. The absence of nematicity is further supported by the angle-resolved photoemission spectroscopy (ARPES) measurements, with no d_{xz}/d_{yz} band splitting observed around the Brillouin zone (BZ) corners. In addition, the band structure around the BZ center is significantly altered for tetragonal HID FeSe_{1-y}Te_y, as compared with the previous reports for tetragonal FeSe_{1-y}Te_y with higher Te contents ($y > 0.5$). Our observations support that the highly mobile electron state emerging in the nematic regime does not contribute to the superconductivity. Interestingly, a ubiquitous dip-like temperature dependence of the Hall coefficient is observed around a characteristic temperature T^* in the tetragonal regimes, which is well above T_c . More importantly, we find that the superconducting transition temperature T_c is closely coupled to the Hall-dip temperature T^* across the FeSe_{1-x}S_x and FeSe_{1-y}Te_y systems. Therefore, our results suggest that the underlying physics setting in at higher temperature in tetragonal background is fundamental for the origin of unconventional superconductivity in the multiband iron-based compounds.

- *Sample description.* FeSe_{1-y}Te_y single crystals with $y = 0.04, 0.06, 0.11, 0.16, 0.22$ and 0.30 were obtained through the soft-chemical HID process¹⁴ (see also Supplementary Fig. S1). The as-grown HID FeSe_{1-y}Te_y crystals are large in size (up to 14 mm; Supplementary Fig. S1c) and free from the chemical phase separation as present in the polycrystalline samples¹². This allows us to readily identify the chemical phase and measure the intrinsic physical properties. The chemical compositions of all the samples were determined by inductively coupled plasma-atomic emission spectrometry. A monotonic, continuous crystal-lattice contraction from FeSe_{1-y}Te_y to FeSe_{1-x}S_x with decreasing y or increasing x was confirmed by x-ray diffraction (XRD) measurements. This is in agreement with the decrease of the ionic radius from Te, Se to S, and indicates that a continuous isovalent substitution is achieved. Correspondingly, a monotonic increase in the chemical compressive stress is expected from FeSe_{1-x}Te_x to FeSe_{1-y}S_y. All our single crystals exhibit a single preferred (001) orientation. The superconducting transition was characterized by both the magnetic susceptibility (χ) and

in-plane resistivity (ρ) measurements, with the T_c value determined from the onset temperature of the superconducting shielding signal in $\chi(T)$. The SC transition is sharp, with the width $\Delta T_c \leq 1$ K for $\text{FeSe}_{1-y}\text{Te}_y$ samples (except for a $\Delta T_c \sim 1.7$ K of $y = 0.30$ with the lowest T_c), and $\Delta T_c \leq 0.5$ K for $\text{FeSe}_{1-x}\text{S}_x$ samples. All the single crystals display a 100 % or large (~ 80 % for $y = 0.30$) superconducting shielding signal, demonstrating their bulk superconductivity. All the details can be found in Supplementary Figs. S3-5.

- **Nematicity and ARPES results.** The S-substituted $\text{FeSe}_{1-x}\text{S}_x$ undergoes a tetragonal to orthorhombic/nematic phase transition upon cooling to T_s . The value of T_s is reduced with increasing substitution x , from maximal $T_s \sim 90$ K at $x = 0$ (FeSe) to ~ 35 K at $x = 0.16$, and finally vanishes at $x \gtrsim 0.17$ (refs. 19-21). The orthorhombic/nematic transition has been shown to manifest itself in many experiments, including a jump or kink at T_s in the T -dependent specific heat (Fig. 1b) or resistivity (Fig. 2d-f), respectively, and a drop in the Hall coefficient at T' just below T_s (Fig. 2j-l). Recently, the nematic transition has been reported in CVT-grown $\text{FeSe}_{1-y}\text{Te}_y$ ($y \lesssim 0.4$) single crystals from the resistivity kink^{22,23} and Hall-coefficient drop²², where T_s decreases with increasing y . However, in our HID-grown $\text{FeSe}_{1-y}\text{Te}_y$ ($0.04 \leq y \leq 0.30$) single crystals, none of the specific-heat jump (Fig. 1a), resistivity kink (Fig. 3a-c), and Hall-coefficient drop (Fig. 3g-i) characteristic of the transition is observed. The presence of the tetragonal phase down to the lowest measuring temperature has also been reported in other iron chalcogenide superconductors, such as binary charge-doped Fe_{1-x}Se (ref. 24) and molecule-intercalated high- T_c (~ 42 K) $(\text{Li}_{1-x}\text{Fe}_x\text{OH})\text{FeSe}$ (ref. 25).

Then, we present the low- T (6 K) electronic structures measured by ARPES for the representative HID $\text{FeSe}_{1-y}\text{Te}_y$ at $y = 0.22$ and CVT $\text{FeSe}_{1-x}\text{S}_x$ at $x = 0.13$, shown in Fig. 3. As can be seen from Fig. 4, the tetragonal $\text{FeSe}_{0.78}\text{Te}_{0.22}$ is intermediate between the strongly nematic FeSe (x or $y = 0$) and optimal- T_c tetragonal $\text{FeSe}_{1-y}\text{Te}_y$ ($y = 0.5$), while the optimal- T_c nematic $\text{FeSe}_{0.87}\text{S}_{0.13}$ is away from FeSe in the other side at a comparable substitution interval. The Fermi-surface mapping is shown in Fig. 3a for $\text{FeSe}_{0.87}\text{S}_{0.13}$ and 3b for $\text{FeSe}_{0.78}\text{Te}_{0.22}$, where dashed blue/red lines mark the Γ - M_1 high-symmetry cuts. The intensity plots of

$\text{FeSe}_{0.87}\text{S}_{0.13}$ around the Γ - and M_1 -point are presented in Fig. 3c and 3e, respectively. The observed hole- and electron-like bands are guided by dashed curves in Fig. 3d (MDC second derivative; MDC: momentum distribution curve) and 3f (EDC second derivative; EDC: energy distribution curve). The Fermi level (E_F) crossings of the hole (α) and electron (δ) bands are demonstrated by the MDCs at E_F , the blue curves in the upper parts of Fig. 3c and 3e, respectively. The band structures around both Γ - and M_1 -point for $\text{FeSe}_{0.87}\text{S}_{0.13}$ are consistent with previous ARPES results⁴⁻⁹. In accordance with the previous orbital-character assignments, the hole-bands α/β near Γ and α'/β' near M_1 (ref. 9) are dominated by Fe d_{xz}/d_{yz} orbital characters, the hole-band γ near Γ by the d_{xy} orbital character. The corresponding spectra of $\text{FeSe}_{0.78}\text{Te}_{0.22}$ are shown in Fig. 3g/h (Γ -cut) and 3i/j (M_1 -cut), with the bands marked by solid curves in Fig. 3h/j. The hole-band ε and electron-band κ cross the Fermi level near Γ and M_1 , respectively, as demonstrated by the MDCs at E_F (red curves in the upper parts of Fig. 3g and 3i). The electron-band κ is more clearly visible from the M_2 -cut data (Supplementary Fig. S6c). The splitting of d_{xz}/d_{yz} bands around the M_1 -point has been widely used to identify the orbital-nematic order⁴⁻⁹, as shown in Fig. 3e/f/k for the present nematic $\text{FeSe}_{0.87}\text{S}_{0.13}$. The corresponding splitting energy Δ_M can be estimated from the EDC at the M_1 -point (blue curve in Fig. 3k). By comparison, the band structure around M_1 for the tetragonal HD $\text{FeSe}_{0.78}\text{Te}_{0.22}$ (Fig. 3i/j/k) is similar to that^{26,27} reported previously for the tetragonal ($y \geq 0.5$; ref. 28) flux $\text{FeSe}_{1-y}\text{Te}_y$ samples. Therefore, the ARPES results support the specific heat and electrical transport characterizations for the presence ($\text{FeSe}_{0.87}\text{S}_{0.13}$) or absence ($\text{FeSe}_{0.78}\text{Te}_{0.22}$) of the nematicity.

Previous ARPES studies^{26,27,29} of tetragonal $\text{FeSe}_{1-y}\text{Te}_y$ with $y > 0.5$ have revealed three hole-bands around Γ in the vicinity of E_F . In the present tetragonal $\text{FeSe}_{0.78}\text{Te}_{0.22}$, we identify only two of them with the d_{xz}/d_{yz} orbital characters, marked as ε/η here; a third hole-band (d_{xy}) is not discernible. The ε (d_{xz}) and η (d_{yz}) hole-bands are resolved by the MDC second derivative around Γ -cut (Fig. 3h) and the overall EDC second derivative along Γ - M_1 direction (Fig. 3l), respectively. We find that, compared to the previous ARPES results, the η (d_{yz}) hole-band does not cross the Fermi level, such that the two hole-bands η (d_{yz}) and ε (d_{xz}) cross at ~ 50 meV below E_F (Fig. 3h/l). These characteristics of band structure around Γ differ from

the previous observations of the highly substituted $\text{FeSe}_{1-y}\text{Te}_y$ (refs. 26,27,29). Therefore, our results indicate that reducing the Te content in tetragonal $\text{FeSe}_{1-y}\text{Te}_y$ mainly affects the band structure around the Γ point, while that around the M points is not significantly altered.

- Hall and resistivity results. Now we switch to an overall view of the in-plane transport data measured for the $\text{FeSe}_{1-x}\text{S}_x$ and $\text{FeSe}_{1-y}\text{Te}_y$ single crystals. The temperature-dependent Hall coefficient $R_H(T)$ of both HID $\text{FeSe}_{1-y}\text{Te}_y$ (Fig. 2g-i) and CVT $\text{FeSe}_{1-x}\text{S}_x$ (Fig. 2j-l) shows a dip around a characteristic temperature T^* in their tetragonal regimes, featuring an obvious upturn in $R_H(T)$ below T^* . $R_H(T)$ of tetragonal HID $\text{FeSe}_{1-y}\text{Te}_y$ keeps on rising with cooling below the Hall-dip T^* (Fig. 2g-i). In contrast, $R_H(T)$ of nematic $\text{FeSe}_{1-x}\text{S}_x$ exhibits a complex behavior consistent with previous observations³⁰⁻³²: The rising trend below T^* collapses to a dramatic drop starting at T' (Fig. 2j-l). Here we emphasize that the Hall-drop T' is slightly below the structural T_s (Fig. 2j-l; Fig. 4). In highly substituted tetragonal $\text{FeSe}_{1-y}\text{Te}_y$ samples, the Hall coefficient generally displays persistent positive values³³ (see also Supplementary Fig. S9), with weakly negative $R_H(T)$ values observed only in a very limited region at low T (refs. 33,34). In their tetragonal regimes, all the $\text{FeSe}_{1-x}\text{S}_x$ and $\text{FeSe}_{1-y}\text{Te}_y$ samples exhibit a linear Hall resistivity $\rho_{xy}(H)$ (Supplementary Figs. S8-9), consistent with the previous results and the nearly compensated metal character^{30,31,35,36}. In the nematic regime of $\text{FeSe}_{1-x}\text{S}_x$, a nonlinearity in $\rho_{xy}(H)$ develops below T' (Supplementary Fig. S8), accompanying the drop in Hall coefficient (Fig. 2j-l). This deviation from the linear $\rho_{xy}(H)$ has been attributed to the emergence of an additional small and highly mobile electron pocket associated with the nematicity^{30,35}.

The in-plane resistivity $\rho(T)$ of $\text{FeSe}_{1-x}\text{S}_x$ samples shows a metallic behavior over the whole measuring temperature range (Fig. 2d-f), similar to previous reports^{30,32,37-39}. By comparison, a broad hump appears in $\rho(T)$ of HID $\text{FeSe}_{1-y}\text{Te}_y$ samples (Fig. 2a-c), and the hump position seems to shift to lower temperature with increasing y . This crossover to non-metallic behavior with heating is similar to the crossover observed previously by ARPES at $y = 0.56$, ascribed to a strong orbital-dependent band renormalization²⁷. Here a noticeable non-metallic upturn also develops in the low- T resistivity of the HID samples at higher y

levels (see Fig. 2c for $y = 0.22$). The extrapolated residual resistivity for the nematic $\text{FeSe}_{1-x}\text{S}_x$ samples is at least one order of magnitude smaller than that for the tetragonal $\text{FeSe}_{1-y}\text{Te}_y$ samples at $y \geq 0.5$. For example, the residual resistivity is only $0.016 \text{ m}\Omega\cdot\text{cm}$ for the present optimal- T_c nematic $\text{FeSe}_{1-x}\text{S}_x$ ($x = 0.13$), while that for the previous optimal- T_c tetragonal $\text{FeSe}_{1-y}\text{Te}_y$ ($y = 0.5$)³⁴ is about $0.16 \text{ m}\Omega\cdot\text{cm}$. Therefore the impurity/defect scatterings are much weaker in the nematic $\text{FeSe}_{1-x}\text{S}_x$ samples.

- Phase diagram and discussion. In Fig. 4, we plot the temperature vs. substitution (x, y) phase diagram of the $\text{FeSe}_{1-x}\text{S}_x$ ($0.19 \geq x \geq 0.0$) and $\text{FeSe}_{1-y}\text{Te}_y$ ($0.04 \leq y \leq 1.0$) systems, by summarizing the present characterizations and some related data from literature. The normal-state region is superimposed with a contour plot of the Hall coefficient. This joint phase diagram clearly shows a double-dome-like evolution of T_c , maximized at $x = 0.13$ ($T_c = 10.8 \text{ K}$) for $\text{FeSe}_{1-x}\text{S}_x$ and at $y \sim 0.5$ ($T_c = 14.4 \text{ K}$; ref. 40) for $\text{FeSe}_{1-y}\text{Te}_y$. Similar superconducting dome of $\text{FeSe}_{1-x}\text{S}_x$ has also been reported in earlier work³⁷.

In the nematic regime ($0.17 \gtrsim x \geq 0$), the electronic nematicity of $\text{FeSe}_{1-x}\text{S}_x$ is enhanced with decreasing x (ref. 7). Both the structural T_s and Hall-drop T' rise correspondingly, reaching their maximal values at stoichiometric FeSe. This trend is also followed by a temperature scale slightly below T' (the white/zero contour line), at which the Hall coefficient changes sign from positive to negative with cooling for $0.1 \gtrsim x \geq 0$. Moreover, a higher T' corresponds to a more negative $R_H(T)$ value at low T (see also Fig. 2j-l). These observations support that the emergence of the high-mobility electron carriers below the Hall-drop temperature T' is inherently connected with the nematic ordering^{30,35}. In the superconducting state, as the system is tuned to cross the boundary ($x \sim 0.17$) into the nematic regime, T_c of $\text{FeSe}_{1-x}\text{S}_x$ rises initially with decreasing x then starts to decline at $x = 0.13$, compared to the continuous enhancement of the nematicity. As crossing from the strongly nematic FeSe at $x = 0$ into the tetragonal HID $\text{FeSe}_{1-y}\text{Te}_y$ region, T_c continues to decline smoothly with increasing y . That is, the changing rate of T_c with substitution remains the same as crossing the $\text{FeSe}_{1-x}\text{S}_x/\text{FeSe}_{1-y}\text{Te}_y$ boundary, despite the sudden disappearance of the high-mobility electron state (as characterized by the concurrently vanishing structural T_s and

Hall-drop T' upon entering the tetragonal region). These observations suggest that the highly mobile electron channel associated with the nematicity does not contribute to the superconducting channel, similar to the recent result of charge-doped Fe_{1-x}Se system²⁴.

For most compensated tetragonal $\text{FeSe}_{1-y}\text{Te}_y$ samples, the Hall coefficient is positive at low T near T_c , indicating the hole dominance. Particularly for tetragonal HID samples showing no Hall-drop T' , the value of Hall coefficient becomes strongly positive towards T_c . We find that T_c of HID $\text{FeSe}_{1-y}\text{Te}_y$ is increased with the enhancement of the positive $R_H(T)$ near T_c (see Fig. 2g-i). This highlights the hole component relevance to the superconductivity. In nematic $\text{FeSe}_{1-x}\text{S}_x$, however, such a strong hole dominance near T_c otherwise seen by the Hall measurement turns out to be either significantly weakened (the light red contour near $x = 0.13$), or completely blanketed (the blue contour for $0.13 > x \geq 0$), by the emergent high-mobility electrons below Hall-drop T' . Since the highly mobile electron state developing at the lower temperature in the nematic regime does not contribute to the superconductivity, the respective roles in the superconductivity played by the nearly compensated holes and electrons, already existing at higher temperatures in the tetragonal regimes, both deserve in-depth investigation. Additionally, in tetragonal high- T_c $(\text{Li}_{1-x}\text{Fe}_x\text{OH})\text{FeSe}$ system with the compensated character manifesting as a persistent electron dominance^{25,41,42}, it has also been shown that both the electrons and holes could contribute to the superconductivity⁴².

Furthermore, the phase diagram reveals a close resemblance between the double-dome shape of T_c and the non-monotonic evolution of T^* in the tetragonal regimes, across the $\text{FeSe}_{1-x}\text{S}_x$ and $\text{FeSe}_{1-y}\text{Te}_y$ systems. Namely, the superconducting transition temperature T_c is pushed up as the Hall-dip temperature T^* is increased. It is noteworthy that a similar T_c scaling with T^* has also been observed in a series of single-crystalline films⁴² and single crystal⁴¹ of high- T_c $(\text{Li}_{1-x}\text{Fe}_x\text{OH})\text{FeSe}$. In Fig. 5, we show the positive correlations between T_c and T^* found in the three iron chalcogenide systems. At higher T^* , the $(\text{Li}_{1-x}\text{Fe}_x\text{OH})\text{FeSe}$ intercalates display much higher T_c/T^* ratios than the isoelectronic samples, likely due to the enhanced extra doping effect from the interlayers as the charge reservoir²⁵. Nevertheless, as T^* is reduced, the extrapolated T_c values of all the three systems approach zero as well.

Therefore, this ubiquitous close link between the superconducting T_c and Hall-dip T^* implies that some generic ingredients essential for superconductivity have developed around T^* in the tetragonal regimes, well above T_c . It is also important to note here that, in our earlier study of the highly two-dimensional high- T_c ($\text{Li}_{1-x}\text{Fe}_x\text{OH}$)FeSe single crystal, we have observed a nearly linear magnetic susceptibility (extracted for the iron planes) and a linear in-plane resistivity, pointing to the presence of magnetic fluctuations^{41,43} as further evidenced by later inelastic neutron scattering experiments^{44,45}. Interestingly, both the linear magnetic susceptibility and resistivity start to appear below the Hall-dip temperature T^* . Here in proximity to the FeTe end, the superconductivity emerges as the AFM order below T_N is suppressed¹. The origin of iron-based superconductivity remains an issue under debate among the scenarios proposed so far, with the proposal of the spin-fluctuation-mediated pairing mechanism as one of them. Previous neutron studies have observed in the tetragonal regimes of both FeSe (at $T > T_s$) (ref. 46) and $\text{FeSe}_{1-y}\text{Te}_y$ (refs. 1,47) the magnetic fluctuations similar to that in iron pnictide superconductors. Further experimental and theoretical studies are certainly needed to pin down the underlying physics setting in below T^* and the connection with the subsequent superconductivity at T_c .

Therefore, our results suggest the tetragonal background to be a fundamental host for the superconductivity. This leads to a straightforward understanding of a partial suppression of superconductivity in the nematic regime. It is obvious that the present nematic $\text{FeSe}_{1-x}\text{S}_x$ ($x = 0.13$) shows an optimal T_c (10.8 K) lower than that ($T_c = 14.4$ K) of the previous optimal tetragonal $\text{FeSe}_{1-y}\text{Te}_y$ ($y = 0.5$); in fact, at a given temperature scale of T^* shared by the isoelectronic samples from the two systems, the nematic $\text{FeSe}_{1-x}\text{S}_x$ samples (blue-shaded area in Fig. 5) consistently exhibit a lower T_c than the tetragonal $\text{FeSe}_{1-y}\text{Te}_y$ samples, despite having the same Hall-dip T^* as, and the much weaker impurity/defect scatterings than, the tetragonal samples. Such a partial suppression of superconductivity is consistent with the recognized irrelevance to superconductivity of the emergent highly mobile electron state, and the reported orbital-selective suppression of possible pairing channels^{9,48}, in the nematic state. Moreover, a twofold-symmetric SC gap has been identified in the nematic FeSe (refs. 49-51)

and $\text{FeSe}_{1-x}\text{S}_x$ (ref. 52), as compared with a modulated fourfold^{53,54} or isotropic^{55,56} SC gap symmetry observed in the tetragonal $\text{FeSe}_{1-y}\text{Te}_y$.

- **Conclusion.** We establish a combined electronic phase diagram of the isoelectronic iron chalcogenides from $\text{FeSe}_{1-x}\text{S}_x$ ($0.19 \geq x \geq 0$) to $\text{FeSe}_{1-y}\text{Te}_y$ ($0.04 \leq y \leq 1.0$). No signature of the electronic nematicity is observed in the HID-grown $\text{FeSe}_{1-y}\text{Te}_y$ ($0.04 \leq y \leq 0.30$) single crystals. We show that reducing the Te content in tetragonal $\text{FeSe}_{1-y}\text{Te}_y$ significantly affects the band structure only around the Γ point. Our observations support that the highly mobile electron state emerging at lower temperature in the nematic regime does not contribute to the superconductivity. We also show that there exists a ubiquitous dip-like temperature dependence of the Hall coefficient around a higher temperature scale T^* in the tetragonal regimes, from the lower- T_c $\text{FeSe}_{1-x}\text{S}_x$ - $\text{FeSe}_{1-y}\text{Te}_y$ systems studied here to a series of iron-chalcogenide intercalates of high- T_c $(\text{Li}_{1-x}\text{Fe}_x\text{OH})\text{FeSe}$ system as reported previously. More importantly, we find that the superconducting transition temperature T_c is pushed up as the Hall-dip temperature T^* is increased in these variants of iron-based superconductors. This ubiquitous close link between T_c and T^* implies that some generic ingredients essential for the superconductivity have developed well above T_c .

Methods

The XRD measurements were carried out at room temperature on an 18 kW MXP18A-HF diffractometer with $\text{Cu-K}\alpha$ radiation, with a 2θ scanning step of 0.01° for the single crystals or 0.02° for the ground powders. The magnetic susceptibility data were measured on a Quantum Design MPMS-XL1 system with a tiny remnant field (< 4 mOe). The in-plane electrical transport measurements were performed on a Quantum Design PPMS-9 system with a six-probe configuration. The Hall signals were determined by subtracting the data in negative fields from that in positive fields with mathematical interpolation. The heat capacity data were measured on the PPMS-9 system by a thermal relaxation method. The ARPES experiments were conducted on a house-made ARPES system (Instrument II) at Center for Correlated Electron System, Institute of Basic Science (Seoul National University, Republic of Korea). The setup was equipped with a SCIENTA DA30 electron analyzer and a Helium discharge lamp as light source (He-I, $h\nu = 21.218$ eV). The total energy resolution was set to be better than 15 meV, and the angular resolution was about 0.5° . The single crystals were cleaved at 5 K and measured at 6 K in an ultrahigh vacuum with basal pressure better than 5×10^{-11} mbar.

Acknowledgements

We would like to thank Drs. L. H. Yang, J. Li, and P. Zheng for technical assistance. This work was supported by the National Key Research and Development Program of China (Grant Nos. 2016YFA0300300 and 2017YFA0303003), the National Natural Science Foundation of China (Grant Nos. 11834016 and 11888101), and the Strategic Priority Research Program and Key Research Program of Frontier Sciences of the Chinese Academy of Sciences (Grant No. QYZDY-SSW-SLH001). The work at SNU was supported by the Institute for Basic Science in Korea (Grant No. IBS-R009-G2).

Reference

- 1 Liu, T. J. et al. From $(\pi,0)$ magnetic order to superconductivity with (π,π) magnetic resonance in $\text{Fe}_{1.02}\text{Te}_{1-x}\text{Se}_x$. *Nat. Mater.* **9**, 716 (2010).
- 2 Zhao, J. et al. Structural and magnetic phase diagram of $\text{CeFeAsO}_{1-x}\text{F}_x$ and its relation to high-temperature superconductivity. *Nat. Mater.* **7**, 953 (2008).
- 3 Kasahara, S. et al. Electronic nematicity above the structural and superconducting transition in $\text{BaFe}_2(\text{As}_{1-x}\text{P}_x)_2$. *Nature* **486**, 382–385 (2012).
- 4 Nakayama, K. et al. Reconstruction of band structure induced by electronic nematicity in an FeSe superconductor. *Phys. Rev. Lett.* **113**, 237001 (2014).
- 5 Shimojima, T. et al. Lifting of xz/yz orbital degeneracy at the structural transition in detwinned FeSe. *Phys. Rev. B* **90**, 121111 (2014).
- 6 Zhang, P. et al. Observation of two distinct d_{xz}/d_{yz} band splittings in FeSe. *Phys. Rev. B* **91**, 214503 (2015).
- 7 Watson, M. D. et al. Suppression of orbital ordering by chemical pressure in $\text{FeSe}_{1-x}\text{S}_x$. *Phys. Rev. B* **92**, 121108 (2015).
- 8 Coldea, A. I. & Watson, M. D. The Key Ingredients of the Electronic Structure of FeSe. *Annu. Rev. Condens. Matter Phys.* **9**, 125 (2018).
- 9 Yi, M. et al. Nematic Energy Scale and the Missing Electron Pocket in FeSe. *Phys. Rev. X* **9**, 041049 (2019).
- 10 Mizuguchi, Y., Tomioka, F., Tsuda, S., Yamaguchi, T. & Takano, Y. Substitution Effects on FeSe Superconductor. *J. Phys. Soc. Jpn.* **78**, 074712 (2009).
- 11 Yeh, K. W. et al. Tellurium substitution effect on superconductivity of the α -phase iron selenide. *EPL* **84**, 37002 (2008).
- 12 Fang, M. H. et al. Superconductivity close to magnetic instability in $\text{Fe}(\text{Se}_{1-x}\text{Te}_x)_{0.82}$. *Phys. Rev. B* **78**, 224503 (2008).
- 13 Yeh, K. W. et al. Superconducting $\text{FeSe}_{1-x}\text{Te}_x$ single crystals grown by optical zone-melting technique. *Cryst. Growth Des.* **9**, 4847–4851 (2009).
- 14 Yuan, D. N. et al. Synthesis of large FeSe superconductor crystals via ion release/introduction and property characterization. *Chin. Phys. B* **25**, 077404 (2016).
- 15 Chareev, D. et al. Single crystal growth and characterization of tetragonal FeSe_{1-x} superconductors. *Cryst. Eng. Commun.* **15**, 1989–1993 (2013).

- 16 Böhmer, A. E. et al. Lack of coupling between superconductivity and orthorhombic distortion in stoichiometric single-crystalline FeSe. *Phys. Rev. B* **87**, 180505 (2013).
- 17 Taen, T., Tsuchiya, Y., Nakajima, Y. & Tamegai, T. Superconductivity at $T_c \sim 14$ K in single-crystalline FeTe_{0.61}Se_{0.39}. *Phys. Rev. B* **80**, 092502 (2009).
- 18 Koshika, Y. et al. Effects of annealing under tellurium vapor for Fe_{1.03}Te_{0.8}Se_{0.2} single crystals. *J. Phys. Soc. Jpn.* **82**, 023703 (2013).
- 19 Hosoi, S. et al. Nematic quantum critical point without magnetism in FeSe_{1-x}S_x superconductors. *Proc. Natl. Acad. Sci. USA* **113**, 8139–8143 (2016).
- 20 Reiss, P. et al. Suppression of electronic correlations by chemical pressure from FeSe to FeS. *Phys. Rev. B* **96**, 121103 (2017).
- 21 Coldea, A. I. et al. Evolution of the low-temperature Fermi surface of superconducting FeSe_{1-x}S_x across a nematic phase transition. *npj Quant. Mater.* **4**, 2 (2019).
- 22 Ovchenkov, Y. A. et al. Nematic properties of FeSe_{1-x}Te_x crystals with a low Te content. Preprint at <http://arxiv.org/abs/1909.00711> (2019).
- 23 Terao, K., Kashiwagi, T., Shizu, T., Klemm, R. A. & Kadowaki, K. Superconducting and tetragonal-to-orthorhombic transitions in single crystals of FeSe_{1-x}Te_x ($0 \leq x \leq 0.61$). *Phys. Rev. B* **100**, 224516 (2019).
- 24 Ni, S. L. et al. Emergence of superconductivity in strongly correlated hole-dominated Fe_{1-x}Se. <http://arxiv.org/abs/1912.12614> (2019).
- 25 Lu, X. F. et al. Coexistence of superconductivity and antiferromagnetism in (Li_{0.8}Fe_{0.2})OHFeSe. *Nat. Mater.* **14**, 325 (2015).
- 26 Chen, F. et al. Electronic structure of Fe_{1.04}Te_{0.66}Se_{0.34}. *Phys. Rev. B* **81**, 014526 (2010).
- 27 Yi, M. et al. Observation of universal strong orbital-dependent correlation effects in iron chalcogenides. *Nat. Commun.* **6**, 7777 (2015).
- 28 Li, S. L. et al. First-order magnetic and structural phase transitions in Fe_{1+y}Se_xTe_{1-x}. *Phys. Rev. B* **79**, 054503 (2009).
- 29 Zhang, P. et al. Multiple topological states in iron-based superconductors. *Nat. Phys.* **15**, 41–47 (2019).
- 30 Watson, M. D. et al. Dichotomy between the hole and electron behavior in multiband superconductor FeSe probed by ultrahigh magnetic fields. *Phys. Rev. Lett.* **115**, 027006 (2015).
- 31 Rößler, S. et al. Emergence of an incipient ordering mode in FeSe. *Phys. Rev. B* **92**, 060505 (2015).
- 32 Sun, Y., Pyon, S. & Tamegai, T. Electron carriers with possible Dirac-cone-like dispersion in FeSe_{1-x}S_x ($x = 0$ and 0.14) single crystals triggered by structural transition. *Phys. Rev. B* **93**, 104502 (2016).
- 33 Sun, Y., Yamada, T., Pyon, S. & Tamegai, T. Influence of interstitial Fe to the phase diagram of Fe_{1+y}Te_{1-x}Se_x single crystals. *Sci.Rep.* **6**, 32290 (2016).
- 34 Zhu, C. S. et al. Tuning electronic properties of FeSe_{0.5}Te_{0.5} thin flakes using a solid ion conductor field-effect transistor. *Phys. Rev. B* **95**, 174513 (2017).
- 35 Huynh, K. K. et al. Electric transport of a single-crystal iron chalcogenide FeSe superconductor: Evidence of symmetry-breakdown nematicity and additional ultrafast Dirac cone-like carriers. *Phys. Rev. B* **90**, 144516 (2014).
- 36 Otsuka, T. et al. Incoherent-coherent crossover and the pseudogap in Te-annealed superconducting Fe_{1+y}Te_{1-x}Se_x revealed by magnetotransport measurements. *Phys. Rev. B* **99**, 184505 (2019).
- 37 Abdel-Hafiez, M. et al. Impurity scattering effects on the superconducting properties and the tetragonal-to-orthorhombic phase transition in FeSe. *Phys. Rev. B* **93**, 224508 (2016).

- 38 Ovchenkov, Y. A., Chareev, D. A., Presnov, D. E., Volkova, O. S. & Vasiliev, A. N. Superconducting properties of $\text{FeSe}_{1-x}\text{S}_x$ crystals for x up to 0.19. *J. Low. Temp. Phys.* **185**, 467–473 (2016).
- 39 Sato, Y. et al. Abrupt change of the superconducting gap structure at the nematic critical point in $\text{FeSe}_{1-x}\text{S}_x$. *Proc. Natl. Acad. Sci. USA* **115**, 1227–1231 (2018).
- 40 Tsurkan, V. et al. Physical properties of $\text{FeSe}_{0.5}\text{Te}_{0.5}$ single crystals grown under different conditions. *Eur. Phys. J. B.* **79**, 289–299 (2011).
- 41 Dong, X. L. et al. $(\text{Li}_{0.84}\text{Fe}_{0.16})\text{OHFe}_{0.98}$ Sesuperconductor: Ion-exchange synthesis of large single-crystal and highly two-dimensional electron properties. *Phys. Rev. B* **92**, 064515 (2015).
- 42 Huang, Y. L. et al. Matrix-assisted fabrication and exotic charge mobility of $(\text{Li,Fe})\text{OHFeSe}$ superconductor films. Preprint at <http://arxiv.org/abs/1711.02920> (2017).
- 43 Dong, X. L., Zhou, F. & Zhao, Z. X. Electronic and superconducting properties of some FeSe-based single crystals and films grown hydrothermally. Preprint at <http://arxiv.org/abs/2009.05731> (2020).
- 44 Pan, B. Y. et al. Structure of spin excitations in heavily electron-doped $\text{Li}_{0.8}\text{Fe}_{0.2}\text{ODFeSe}$ superconductors. *Nat. Commun.* **8**, 123 (2017).
- 45 Ma, M. W. et al. Low-energy spin excitations in $(\text{Li}_{0.8}\text{Fe}_{0.2})\text{ODFeSe}$ superconductor studied with inelastic neutron scattering. *Phys. Rev. B* **95**, 100504 (2017).
- 46 Wang, Q. S. et al. Magnetic ground state of FeSe. *Nat. Commun.* **7**, 12182 (2016).
- 47 Lumsden, M. D. et al. Evolution of spin excitations into the superconducting state in $\text{FeTe}_{1-x}\text{Se}_x$. *Nat. Phys.* **6**, 182–186 (2010).
- 48 Sprau, P. O. et al. Discovery of orbital-selective cooper pairing in FeSe. *Science* **357**, 75–80 (2017).
- 49 Song, C. L. et al. Direct observation of nodes and twofold symmetry in FeSe Superconductor. *Science* **332**, 1410–1413 (2011).
- 50 Liu, D. F. et al. Orbital origin of extremely anisotropic superconducting gap in nematic phase of FeSe superconductor. *Phys. Rev. X* **8**, 031033 (2018).
- 51 Hashimoto, T. et al. Superconducting gap anisotropy sensitive to nematic domains in FeSe. *Nat. Commun.* **9**, 282 (2018).
- 52 Xu, H. C. et al. Highly anisotropic and twofold symmetric superconducting gap in nematically ordered $\text{FeSe}_{0.93}\text{S}_{0.07}$. *Phys. Rev. Lett.* **117**, 57003 (2016).
- 53 Zeng, B. et al. Anisotropic structure of the order parameter in $\text{FeSe}_{0.45}\text{Te}_{0.55}$ revealed by angle-resolved specific heat. *Nat. Commun.* **1**, 112 (2010).
- 54 Okazaki, K. et al. Evidence for a $\cos(4\phi)$ modulation of the superconducting energy gap of optimally doped $\text{FeTe}_{0.6}\text{Se}_{0.4}$ single crystals using laser angle-resolved photoemission spectroscopy. *Phys. Rev. Lett.* **109**, 237011 (2012).
- 55 Nakayama, K. et al. Angle-resolved photoemission spectroscopy of the iron-chalcogenide superconductor $\text{Fe}_{1.03}\text{Te}_{0.7}\text{Se}_{0.3}$: Strong coupling behavior and the universality of interband scattering. *Phys. Rev. Lett.* **105**, 197001 (2010).
- 56 Miao, H. et al. Isotropic superconducting gaps with enhanced pairing on electron Fermi surfaces in $\text{FeTe}_{0.55}\text{Se}_{0.45}$. *Phys. Rev. B* **85**, 094506 (2012).

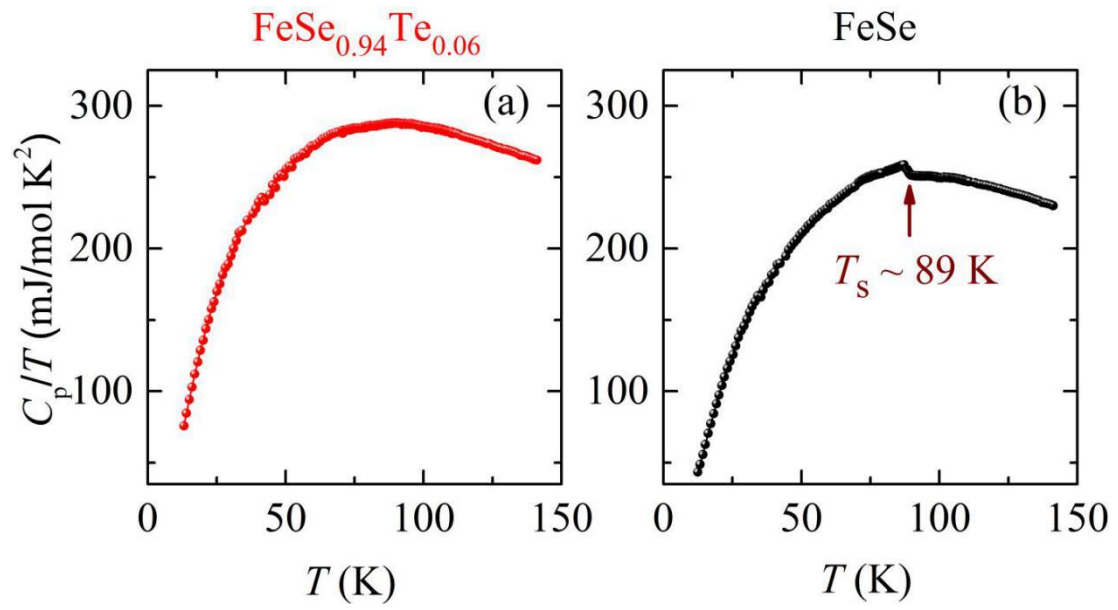


FIG. 1. Temperature dependences of the specific heat for the single crystals of (a) representative tetragonal HID $\text{FeSe}_{0.94}\text{Te}_{0.06}$ and (b) nematic CVT FeSe .

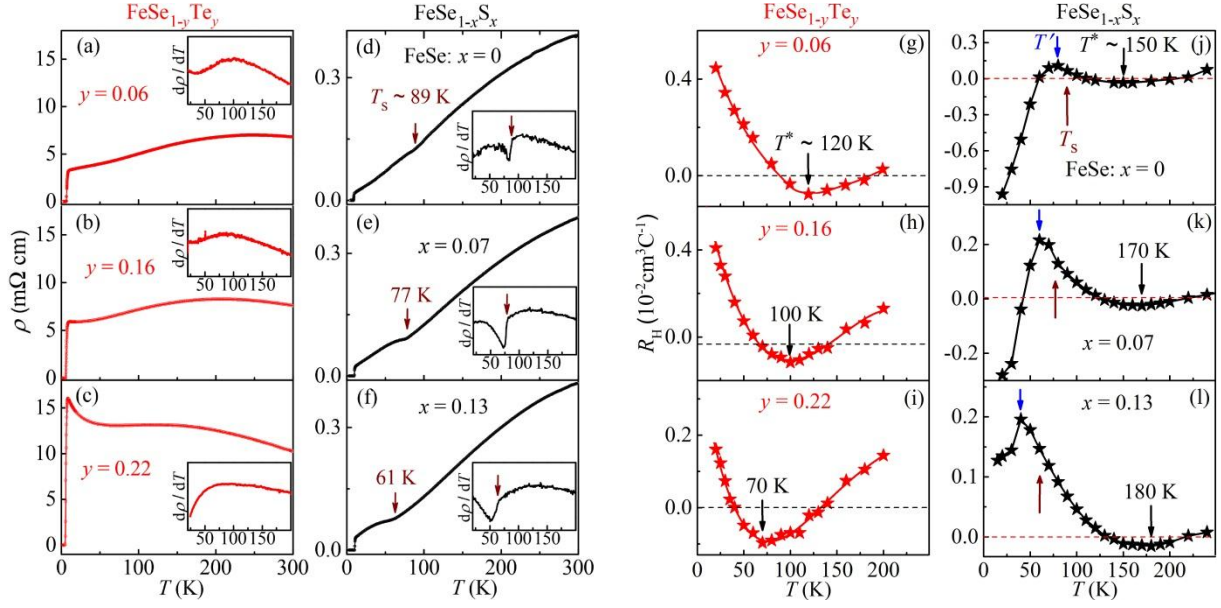


FIG. 2. (a-c) and (d-f) show the temperature-dependent in-plane resistivity for representative tetragonal HID $\text{FeSe}_{1-y}\text{Te}_y$ and nematic CVT $\text{FeSe}_{1-x}\text{S}_x$ single crystals, respectively. The data of $\text{FeSe}_{1-y}\text{Te}_y$ at other Te substitutions are given in Supplementary Fig. S7. Insets: The temperature derivatives of the resistivity exhibit clear drops at T_s for the nematic $\text{FeSe}_{1-x}\text{S}_x$ samples. (g-i) and (j-l) are the temperature-dependent Hall coefficients of these samples, obtained from the fit to the linear Hall resistivity $\rho_{xy}(H)$ or the field derivative of $\rho_{xy}(H)$ at the zero-field limit in the case of nonlinear $\rho_{xy}(H)$. All the $\rho_{xy}(H)$ data are presented in Supplementary Figs. S8-9.

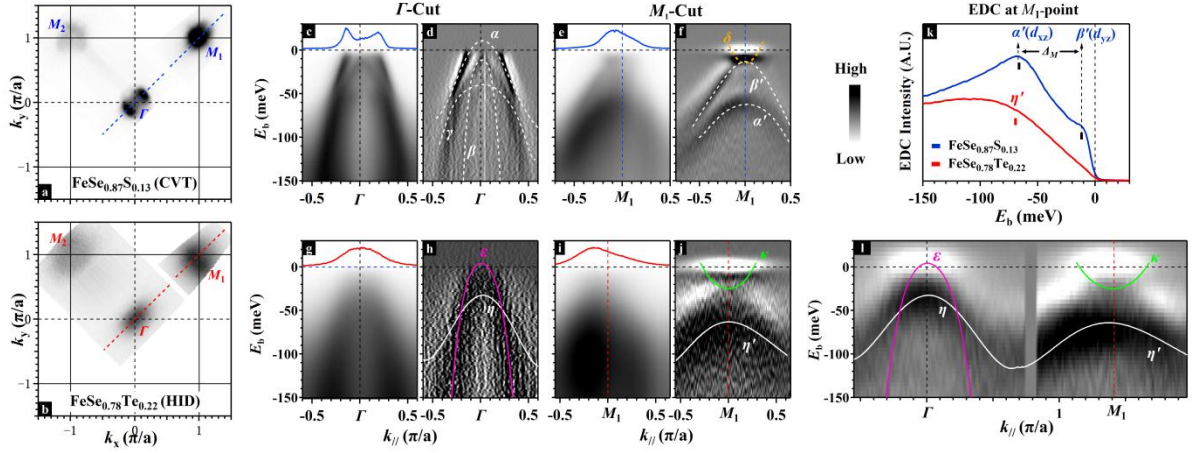
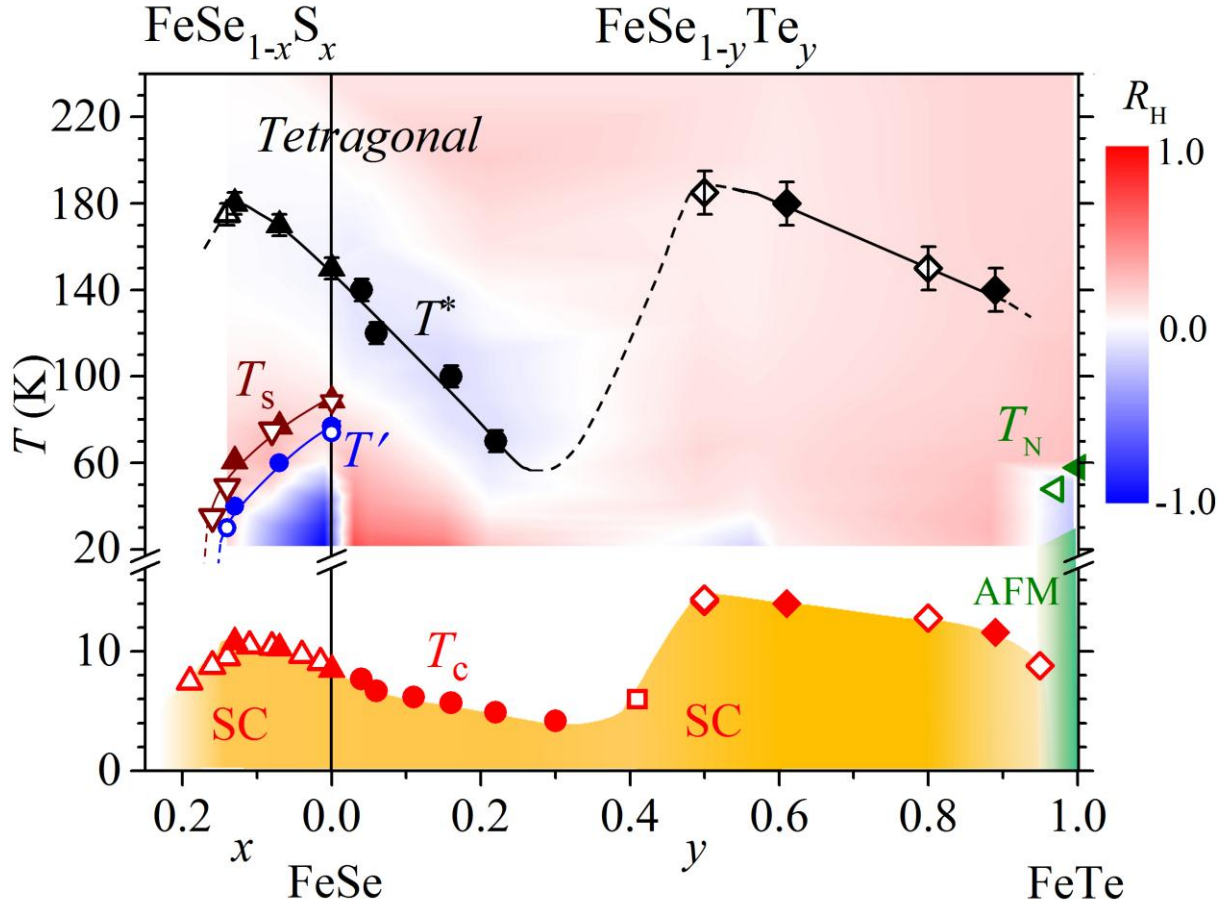


FIG. 3. (a) and (b) show the ARPES Fermi-surface mapping in the 2-Fe BZ for nematic CVT $\text{FeSe}_{1-x}\text{S}_x$ ($x = 0.13$) and tetragonal HID $\text{FeSe}_{1-y}\text{Te}_y$ ($y = 0.22$), respectively. The dashed blue/red lines indicate the Γ - M_1 high-symmetry direction. The intensity plots of $\text{FeSe}_{0.87}\text{S}_{0.13}$ are shown in (c) for the Γ -cut and (e) for the M_1 -cut, with their MDC/EDC second derivatives presented in (d) and (f), respectively. In the upper parts of (c) and (e) are the MDCs at E_F . (g)-(j) show the corresponding data for $\text{FeSe}_{0.78}\text{Te}_{0.22}$. (k) The blue EDC at M_1 characterizes the band splitting energy Δ_M for nematic $\text{FeSe}_{0.87}\text{S}_{0.13}$. (l) Overall EDC second derivative along the Γ - M_1 direction for $\text{FeSe}_{0.78}\text{Te}_{0.22}$. All the ARPES data were measured at $T = 6$ K with $h\nu = 21.218$ eV from He-I discharging.



This work		Literature		This work		Literature	
T_c : ●	HID	□	FZ [13]	T^* : ●	HID	▲	CVT [32]
▲	CVT	△	CVT [32,37]	▲	CVT	△	CVT [32]
◆	Flux	◇	Flux [33,34,36,40]	◆	Flux	◇	Flux [34,36]
T_s : ▲	HID	▽	CVT [32,39]	T' : ●	CVT	○	CVT [32]
T_N : ◀	Flux	◀	Flux [33]				

FIG. 4. T - x/y phase diagram of the $\text{FeSe}_{1-x}\text{S}_x$ and $\text{FeSe}_{1-y}\text{Te}_y$ systems, superimposed by a contour plot of the Hall coefficient R_H in the normal state. The present results are denoted by filled symbols, the data from literature by open symbols. The solid/dashed lines are drawn as guide to the eye. (FZ for the red open square is short for the floating-zone method.)

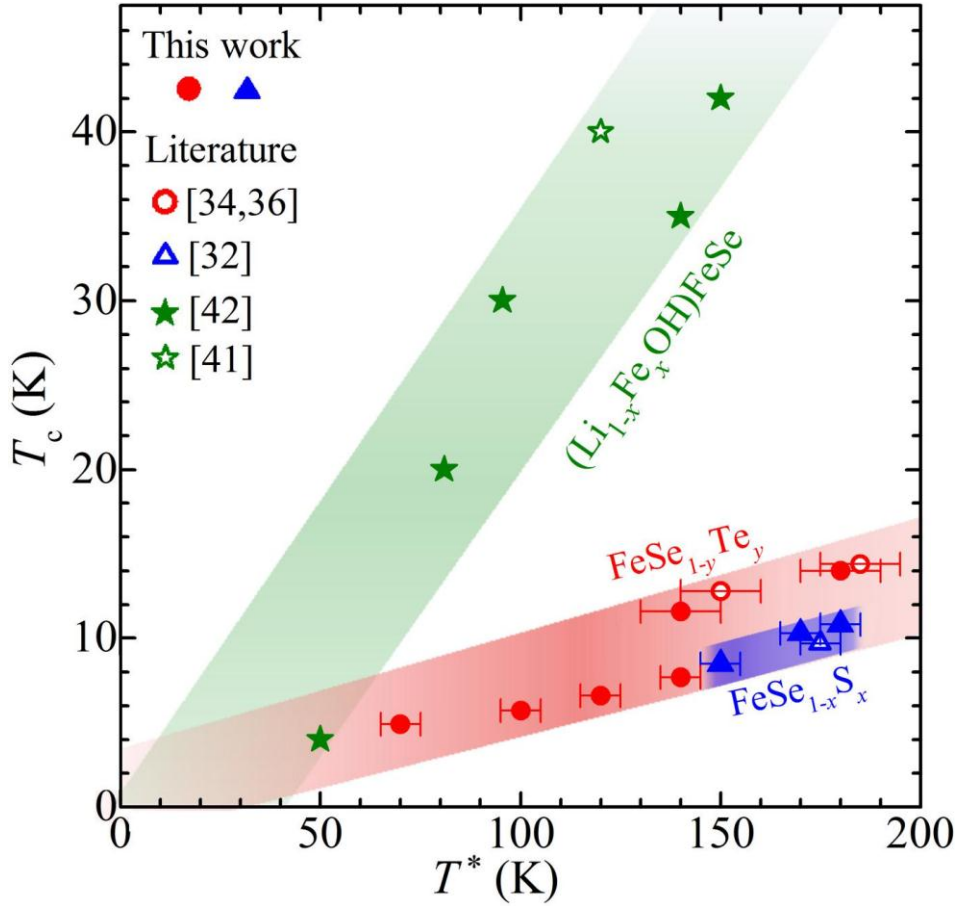


FIG. 5. Positive correlations between the superconducting T_c and Hall-dip T^* observed in the three iron-chalcogenide systems, with the colored shadings showing the trends. The filled/open circles and triangles represent the present/previous results of $\text{FeSe}_{1-y}\text{Te}_y$ and $\text{FeSe}_{1-x}\text{S}_x$ single crystals, respectively. The filled and open stars stand for the previous data of single-crystalline films⁴² and single crystal⁴¹ of high- T_c $(\text{Li}_{1-x}\text{Fe}_x\text{OH})\text{FeSe}$ system, respectively. Note: The T_c values of the films were taken as the zero-resistivity onset temperatures⁴².